Size of heterogeneous deformations in sheared granular flows

Parisa Shekari, Benjy Marks, and Pierre Rognon*
School of Civil Engineering, The University of Sydney, 2006 Sydney, Australia

(Received 5 April 2023; accepted 18 October 2023; published 8 December 2023)

Sheared granular materials spontaneously develop heterogeneous and transient kinematic fields which resemble turbulence. We focus here on characterizing the length scale of these heterogeneities. We simulate plane-shear flows and measure the local grain velocity, velocity fluctuation, shear rate, vorticity, and dilation rate. The results show that these quantities are widely distributed, even more so at low inertial numbers. We relate this effect to spatial correlations that develop at low inertial numbers, where the flow becomes partitioned into "cold" patches with lower than average strain rate and "hot" zones where the strain rate is concentrated. We finally extract a characteristic length scale for the size of these heterogeneities, corresponding to the size of a representative elementary volume. This size is found to vary from a few grain diameters at high inertial number to a few dozen grain diameters at low inertial number, following a characteristic power law. These insights into. representative elementary volume (REV) size may be of importance to further develop continuum models for granular flows, capturing local and nonlocal effects.

DOI: 10.1103/PhysRevFluids.8.124301

I. INTRODUCTION

A continuum description for granular flows is key to predict the behavior of many natural events and industrial processes. This description hinges on continuity equations capturing mass and momentum conservation. Each law relates a diffusion coefficient—diffusivity or viscosity—to spatially averaged deformations and stresses. Examples of such laws include the $\mu(I)$ frictional rheology [1,2], nonlocal models [3–5], and scaling laws for shear-induced diffusion [6–8]. These laws are predicated on the assumption of the existence of a finite size representative elementary volume (REV), which is defined as the minimum volume of material needed to obtain a behavior similar to any larger volume.

The existence of a REV has been demonstrated in granular packings subjected to quasistatic loading, focusing on structural and mechanical properties such as porosity [9], and stress and energy dissipation [10,11]. The size of the REV was found to be influenced by various factors, including the type of material, elastic properties, geometry [10,12,13], boundary conditions [10], and loading patterns [11]. In contrast, the existence and size of REVs in granular flows remains to be established.

While a single grain diameter is an intuitive lower bound for a REV, analysis of granular flow internal kinematics suggest that it could, in fact, be much larger. These studies have revealed the spontaneous development of the correlated motion of grains, a process coined "granulence" by analogy with velocity correlations observed in turbulent flows [14,15]. The structure of these granular clusters yields some mesoscopic length scale which is likely to affect the REV size [16–20]. For example, a configuration that is too small to let granular clusters develop to their full size could behave differently to a larger configuration able to accommodate larger clusters. The drop

*pierre.rognon@sydney.edu.au

in effective viscosity observed near flow boundaries is an empirical confirmation of this relation [21–23].

This work attempts to measure the REV size in granular flow by focusing on their internal kinematics. In discrete element method simulations of plane-shear flows covering a range of inertial numbers (Sec. II), we first measure local quantities including grain velocity, relative velocity (Sec. III), and local velocity gradient tensors (Sec. IV), and analyze their statistical distribution. We then extract a REV size based on the local rate of shear and vorticity (Sec. V), with a particular interest in its variation with the inertial number.

II. PLANE SHEAR FLOWS

We use the discrete element method (DEM) to simulate plane-shear flows of dry, cohesionless grains. The simulated system is presented in Fig. 1(a). It consists of a two-dimensional assembly of 10^4 grains with a mean diameter d, mass m, and density ρ. To prevent shear-induced crystallization, a uniform polydispersity of $d \pm 20\%$ is introduced in the grain diameters. The system is two dimensional (x and y directions only) and Lees-Edwards periodic boundary conditions [24] are used to avoid flow heterogeneity induced by solid walls [22]. The shear rate $\dot{\gamma} = \frac{2u}{H}$ and normal stress P are prescribed and kept constant during flow, where u is the shearing velocity at the boundaries and H is the system size in the y direction, which varies to maintain a constant value of P. The system size in the x direction is kept constant at $100d$.

Grains interact through direct contact via a contact force comprised of a linear elastic repulsion, a viscous dissipation, and tangential friction. The associated mechanical parameters are the normal stiffness $k_n = 10^3 P$, the coefficient of restitution set to 0.5, and the coefficient of friction set to 0.5. The choice of these parameters was found to only mildly influence the rheological behavior of the packing [2,25]. The ratio k_n/P is selected to be as low as possible to enable larger time steps and therefore reduce computational time, while large enough not to affect the flowing properties of the material. It is expected that stiffer grains would yield similar results. In contrast, softer grains could affect the flow dynamics [25], although such highly deformable grains are seldom.

In the absence of gravity, this configuration yields homogeneous, steady shear flows. Here, homogeneous means that when averaged over time, the shear rate $\dot{\gamma}$ and the stresses are the same anywhere in the flow. This implies that the inertial number [1,2] is also homogeneous,

$$I = \dot{\gamma} t_i,$$

where $t_i = d\sqrt{\frac{\rho}{P}}$ is the inertial time. At any point in time, however, local fluctuations may arise, which will be the focus of the analysis below.

A series of steady flows was simulated covering a range of inertial numbers $10^{-3} \leqslant I \leqslant 1$. The lower values correspond to a quasistatic regime, while the higher values correspond to a collisional regime. Each flow is prepared by preshearing an initially loose and random packing over five shear deformations. This is sufficient to reach a steady regime during which macroscopic stresses and solid fractions are no longer evolving. The grain's velocity and position are then recorded every 1/20th of a shear deformation, for a duration of 15 shear deformations. This forms the database analyzed below.

III. GRAIN AND PAIR VELOCITIES

We first consider individual grain velocities, given by $\vec{v}^i$ for the velocity of grain i in the x and y directions, with components v_x^i and v_y^i. We define the nonaffine components $\delta\vec{v}^i$ as

$$\delta v_x^i = v_x^i - y^i \dot{\gamma}, \quad \delta v_y^i = v_y^i. \tag{1}$$

Here, $\delta\vec{v}^i$ measures the deviation from the time-averaged flow field, which is $y\dot{\gamma}$ in the x direction and 0 in the y direction. We refer to $\delta\vec{v}^i$ as the velocity fluctuation. Figures 1(b) and 1(c) illustrate

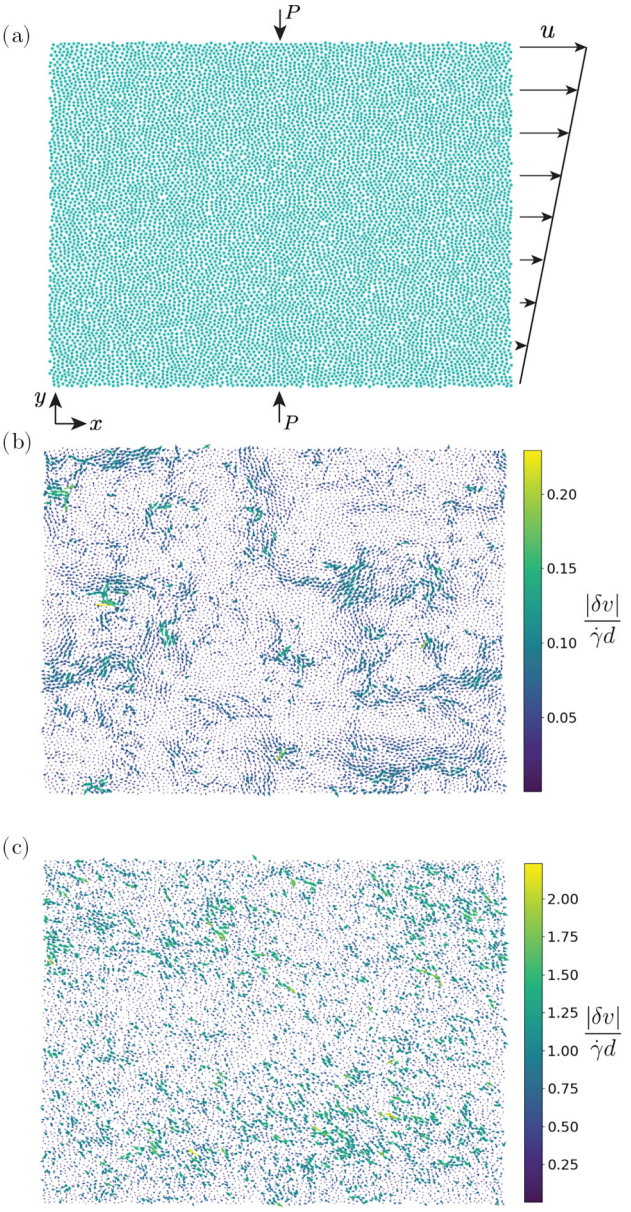

FIG. 1. Velocity fluctuations in plane-shear flows. (a) Schematic of the plane-shear flow configuration, featuring a snapshot of the grain packing under applied pressure P and shear velocity u. The system dimension is $100d \times 80d$. (b),(c) Snapshots of grain velocity fluctuations for inertial numbers $I = 0.01$ and $I = 0.5$, respectively. The arrows represent the velocity fluctuations δv in both the x and y directions for each grain, with the arrow base located at the center of the grain.

fields of velocity fluctuation in two snapshots taken in flows with $I = 0.01$ and $I = 0.5$, respectively. In agreement with previous findings [6,14,26], these snapshots show that grains are not simply following the average flow field. They feature large fluctuations, with some spatial correlations at low inertial number.

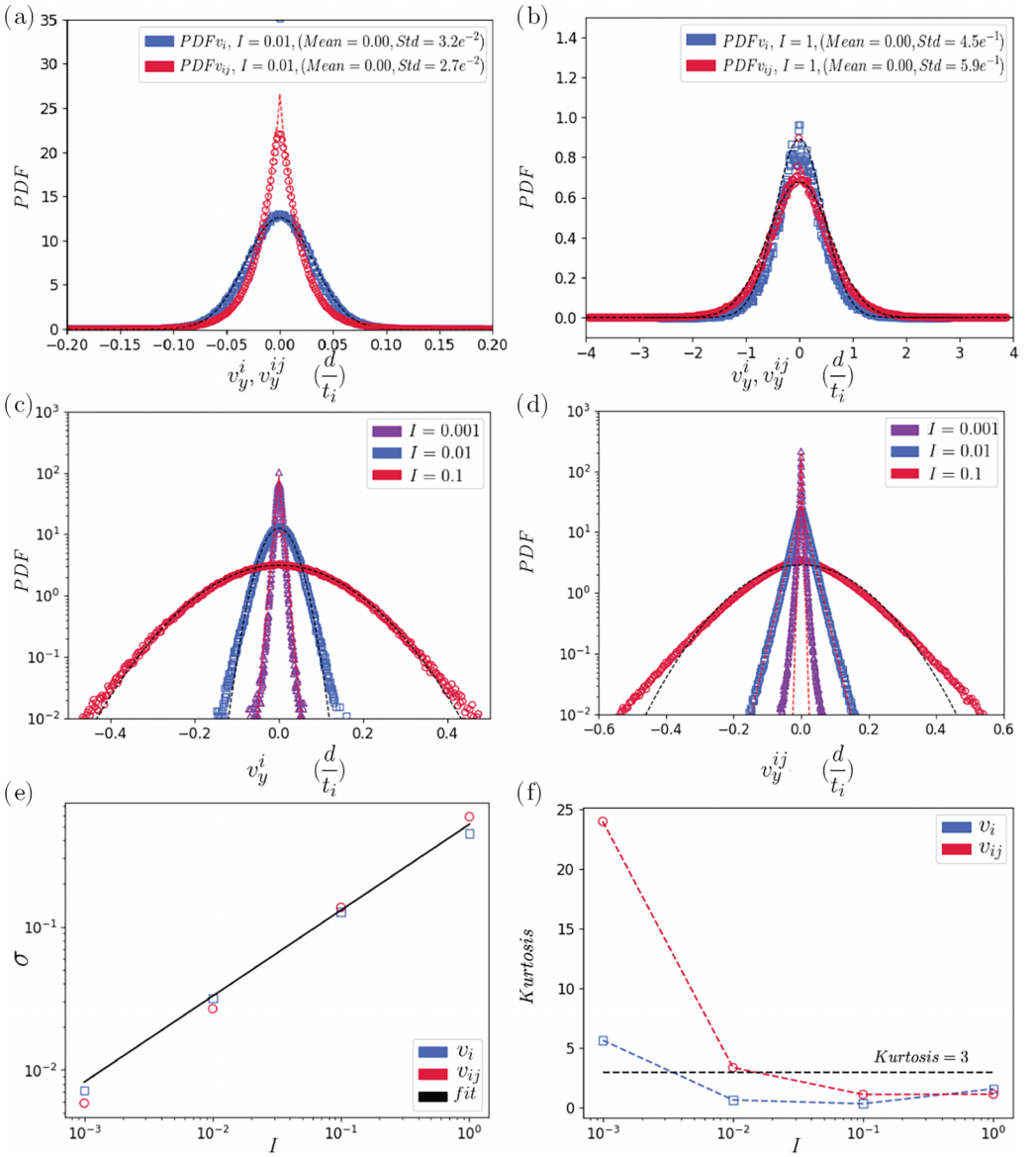

FIG. 2. Velocity and relative velocity distributions in plane-shear flows. (a),(b) Distributions of grain velocity (v_y^i) and grain relative velocity (v_y^{ij}) in the y direction for two different inertial numbers $I = 0.01$ and $I = 1$, respectively. Black lines are normal distribution fits; red line is an exponential distribution fit. Means and standard deviation of the distributions are given in the legends. (c),(d) Distributions of v_y^i and v_y^{ij} for a range of inertial numbers. (a)–(d) Velocities are in units of d/t_i. (e) Standard deviation of velocity fluctuations $\sigma(\delta v_y^i)$ (blue) and $\sigma(\delta v_y^{ij})$ (green) for different inertial numbers I, and power law in Eq. (3) (black line). (f) Kurtosis of v_y^i (blue) and v_y^{ij} (green) for different inertial numbers.

To highlight the existence of cooperative motion suggested in Fig. 1(b), we next consider the relative velocity of pairs of grains in the y direction, defined as

$$\delta v_y^{ij} = v_y^j - v_y^i, \tag{2}$$

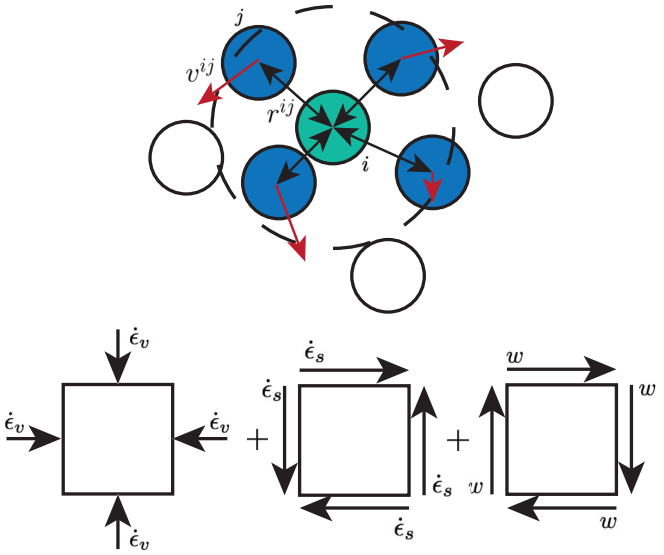

FIG. 3. Velocity gradient and decomposition into deformation rates. Top: Illustration of how the velocity gradient tensor F is calculated for a single grain (green) including close neighbors (blue) using Eq. (4); the calculation involves relative position (r^{ij}) and relative velocity (v_y^{ij}). The cutoff distance used to define neighboring grains in this study is $|r^{ij}| \leqslant 2d$, which is highlighted as the dashed circle. This cutoff distance is chosen to evaluate the velocity gradient on the smallest possible zone while ensuring that enough neighbors are present to determine F. Bottom: Decomposition of the velocity gradient tensor into volumetric strain rate, shear strain rate, and vorticity, corresponding to the trace, symmetric, and antisymmetric parts of F.

for all neighboring pairs of grains i and j. Two grains are deemed neighbors if their center-to-center distance is less than $2d$. Pairs that are farther away are excluded. The rationale for considering pair relative velocities is that their distribution can indicate the presence of spatial correlation within a distance $2d$. In the absence of spatial correlation, grain and pair velocities should be equally distributed. In contrast, some differences in their distribution should arise in the presence of spatial correlation.

Figures 2(a) and 2(b) compare the probability density functions (PDFs) of these two quantities including all grains, all pairs, and all time steps at two inertial numbers $I = 0.01$ and $I = 1$. At high inertial number, grain and pair velocities both follow a normal distribution. At low inertial number, grain velocities follow a normal distribution, while pair velocities follow an exponential distribution. Consistent with the representation in Fig. 1, this suggests the development of spatially correlated motion at low inertial number. This transition, or lack of transition, from a normal to an exponential distribution is further illustrated in Figs. 2(c) and 2(d).

How much the grain and pair velocities deviate from the mean flow—which is null in this direction—is measured by the standard deviation of these distributions, $\sigma(v_y^i)$ and $\sigma(v_y^{ij})$. Figure 2(e) shows that in spite of the difference in the shape of these distributions, standard deviations of grain and pair velocities follow a similar power law of the inertial number,

$$\frac{\sigma(\delta v_y^i)}{d/t_i} \approx \frac{\sigma(\delta v_y^{ij})}{d/t_i} \approx \alpha I^{n_I}. \tag{3}$$

The results are consistent with exponents $n_I \approx 0.60$ and coefficient $\alpha \approx 0.50$. Such a power law for v_i is consistent with previous results [2,8,27]. A power exponent $n_I = 1$ would yield $\delta v_y^{ij} \propto \dot{\gamma} d$, which means that velocity fluctuations are entirely driven by the characteristic shear velocity $\dot{\gamma} d$, with no effect of the inertial time t_i. A power exponent less than 1 means that the two standard

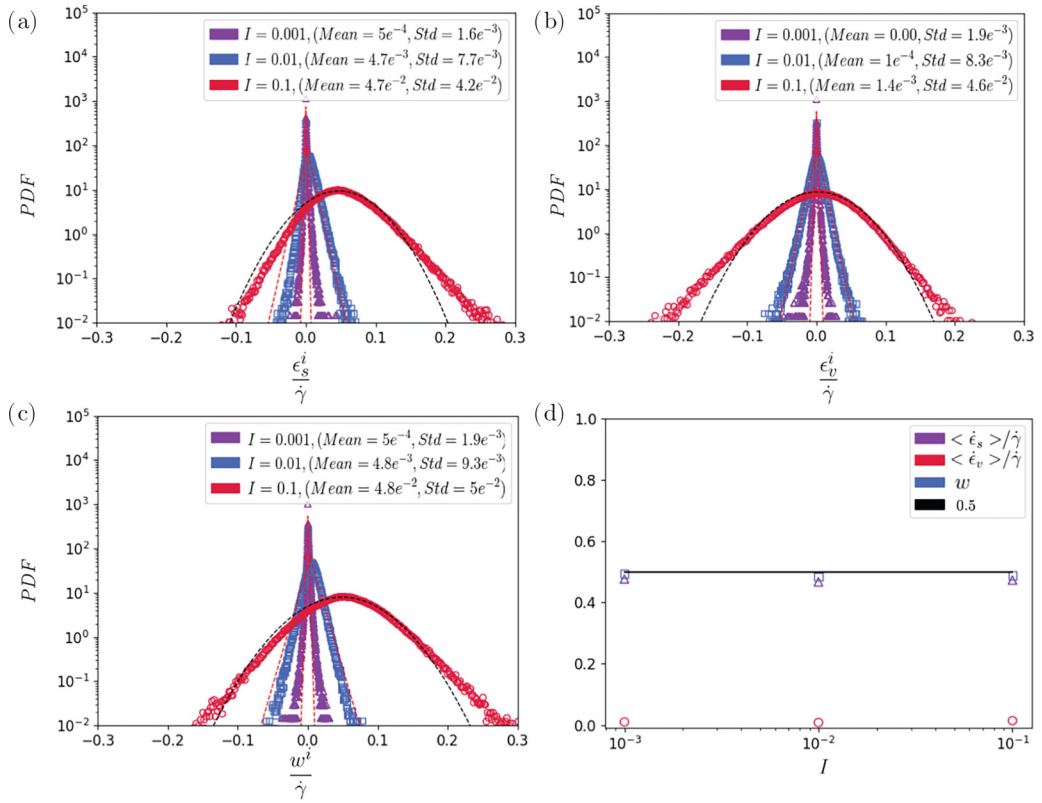

FIG. 4. Distribution of local deformation rates. (a) Shear strain rate ($\dot{\epsilon}_s$), (b) volumetric strain rate ($\dot{\epsilon}_v$), and (c) vorticity (w) for different inertial number I. (a)–(c) Means and standard deviations of the distributions are indicated in the legends. (d) Means $\langle \dot{\epsilon}_s \rangle$ (green line), $\langle \dot{\epsilon}_v \rangle$ (red line), and $\langle w \rangle$ (blue line) of these distributions normalized by the macroscopic shear rate $\dot{\gamma}$, including a black line at 0.5 for visual reference.

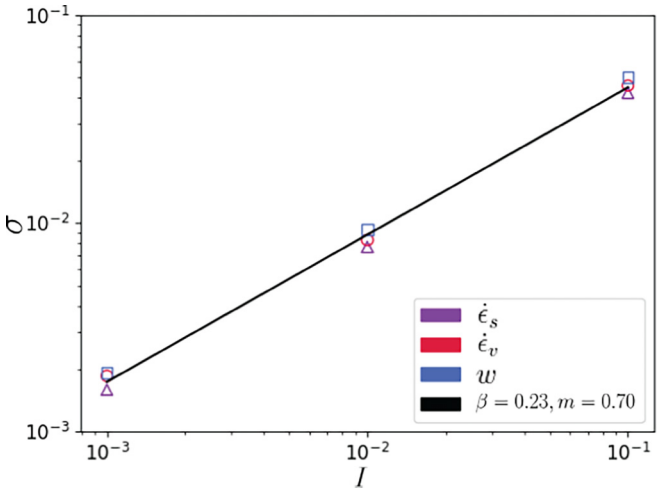

FIG. 5. Fluctuations of deformation rates, represented by the standard deviation of the local shear strain rate $\sigma(\dot{\epsilon}_s)$, volumetric strain rate $\sigma(\dot{\epsilon}_v)$, and vorticity $\sigma(w)$ in unit t_i^{-1} at different inertial number. The black line is the power law in Eq. (6) with $\beta = 0.23, m = 0.70$.

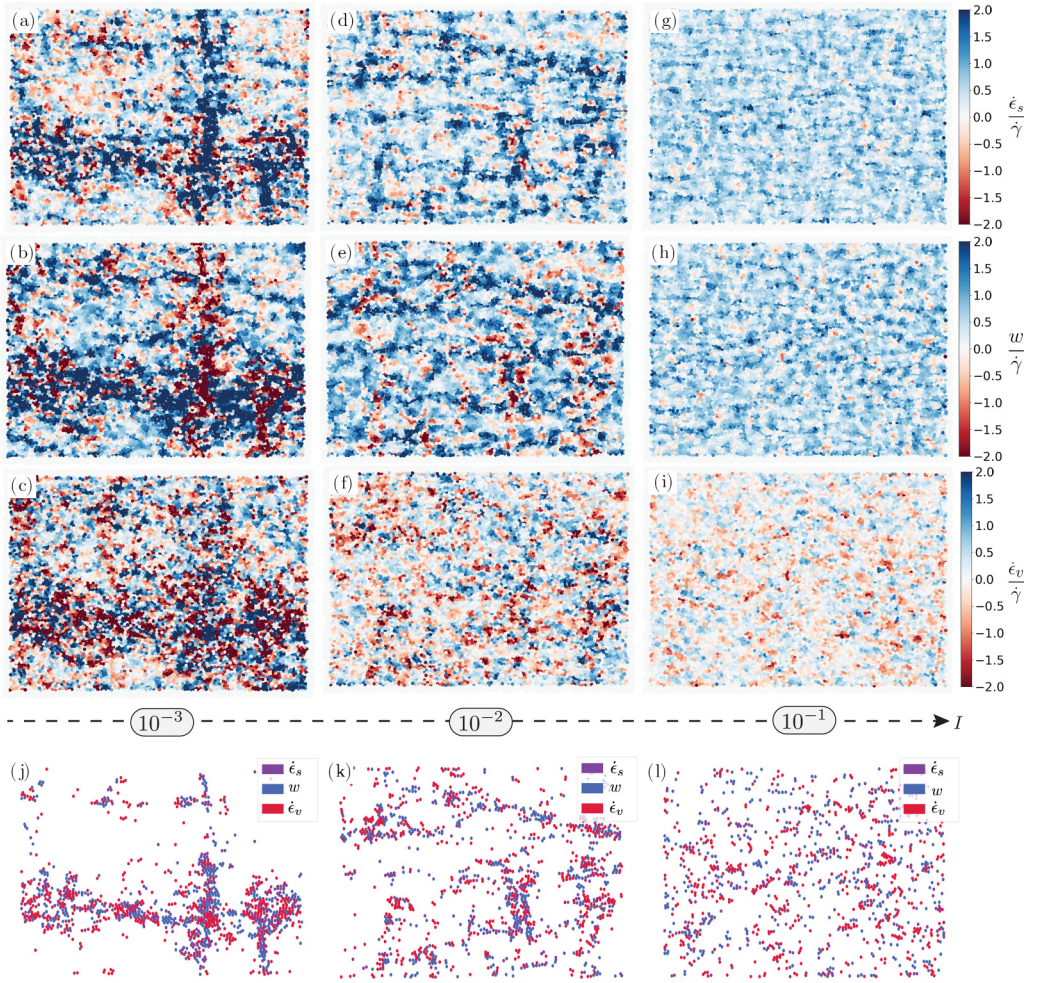

FIG. 6. Spatial distribution of kinematic fields. (a)–(i) Normalized shear strain rate, volumetric strain rate, and vorticity fields at three different inertial numbers $I = 0.001$, $I = 0.01$, and $I = 0.1$, respectively. (j)–(l) Spatial distribution of extreme values in each kinematic field at the same inertial numbers.

deviations become sensitive to the inertial time t_i and are much larger than the characteristic shear velocity $\dot{\gamma} d$ at low inertial numbers. A qualitative interpretation is that velocity fluctuations become driven by inertial rearrangements, which characteristic time t_i is independent of the shear time $\dot{\gamma}^{-1}$.

Compared to a normal distribution, an exponential distribution features higher probability near the mean value—zero in our case—and a higher probability very far from the mean. The transition from a normal to an exponential distribution for the pair velocities can then be understood as resulting from a partitioning of the flow into (i) "cold" zones with low pair velocities comprised of most pairs, and (ii) "hot" zones with high pair velocities comprised of few outlier pairs. The measure of the kurtosis of these distributions, shown in Fig. 2(f), further highlights the increasing presence of outliers at low inertial number. For individual grain velocity, the value of the kurtosis remains near 3, which is the value expected for a normal distribution. In contrast, pair velocity distributions exhibit significant excess kurtosis, with values reaching 25 at the lower inertial number. These high values are driven by, and thus reflect the increasing presence of, outliers in these distributions.

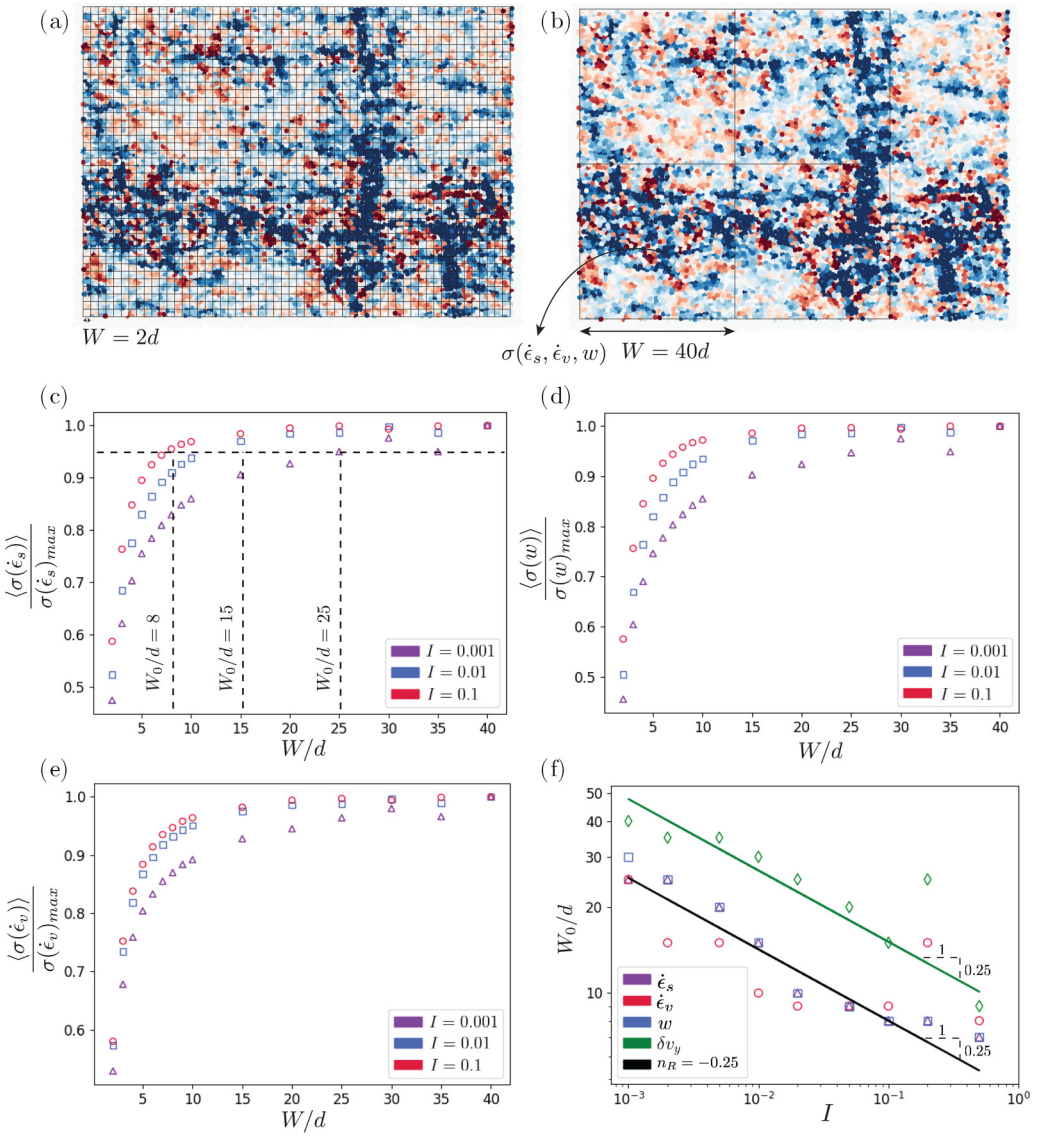

FIG. 7. REV size. (a),(b) Illustrations of the window size (W $= 2d$ and $40d$) used to measure standard deviations σ of kinematic quantities, and the mean of these standard deviations $\langle\sigma\rangle$ including all windows and all times. (c)–(e) Evolution of the mean standard deviation as a function of the window size W, normalized by its maximum value defined as $\sigma_{\max} = \langle\sigma\rangle(W = 40d)$. Dashed lines on (c) show the method used to extract a minimum REV size W_0 for different inertial numbers. (d) Minimum REV size W_0 obtained from shear strain rate, volumetric strain rate, and vorticity velocity fluctuation in the y direction, as a function of the inertial number. The green and black lines correspond to the power law in Eq. (7).

IV. VELOCITY GRADIENT AND DEFORMATION RATE

The heterogeneity in grain and pair velocities evidenced above suggests that the rate of deformation within the flow is also not homogeneous and is likely to deviate from the macroscopic shear rate $\dot{\gamma}$. To evidence heterogeneities in the deformation rate, we measured the local velocity gradient

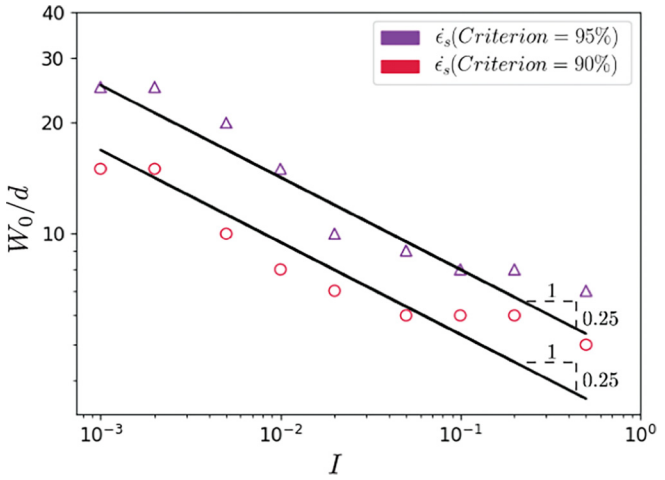

FIG. 8. Effect of criterion on REV. REV size of shear strain rate for two criteria of 95% and 90%. Lines are best fit using Eq. (7).

tensor defined for each grain as [22,28]

$$F^i = \langle r^{ij} \otimes r^{ij} \rangle^{-1} \cdot \langle r^{ij} \otimes v^{ij} \rangle. \tag{4}$$

The symbols $\cdot$ and $\otimes$ denote the tensor product and the outer product, respectively, and $^{-1}$ represents the inverse of the tensor. $\langle \cdot \rangle$ represents an average over all pairs of neighboring grains j; and r^{ij} is the center-to-center vector between two grains and v^{ij} their relative velocity vector. Pairs are considered neighbors if their center-to-center distance is less than $2d$. F^i is a second-rank tensor that measures a spatial average of the velocity gradient in this zone, as illustrated in Fig. 3. The distance $2d$ is chosen to be as small as possible to obtain local information while ensuring that enough neighbors are included to evaluate the velocity gradient.

In the following, we will focus on three kinematic quantities extracted from this tensor: the shear strain rate $\dot{\epsilon}_s^i$ (symmetric part of F), the vorticity w^i (antisymmetric part of F), and the volumetric

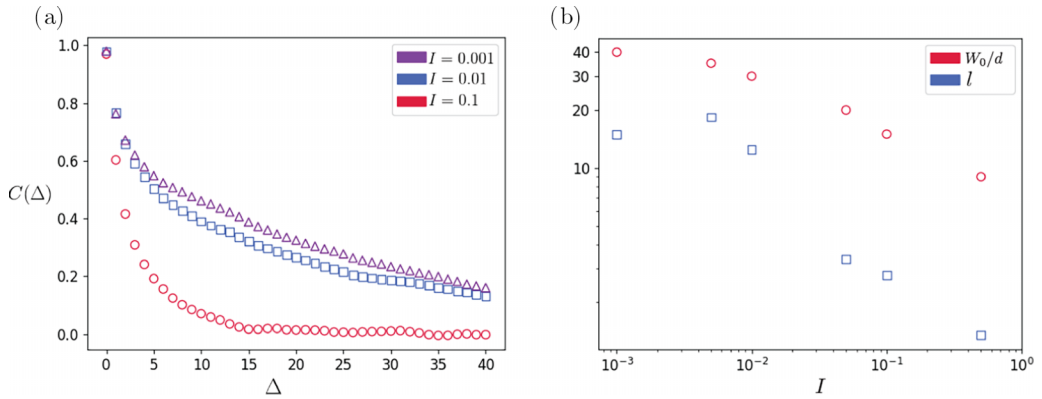

FIG. 9. Spatial correlation of v_y. (a) The dependence of the v_y spatial correlation to the controlling parameter $\Delta(d)$, where d is the average diameter of the grains. (b) The comparison between the extracted minimum REV size W_0/d and correlation length (l) obtained from v_y for different inertial numbers.

strain rate $\dot{\epsilon}_v^i$ (trace of F), defined as

$$\dot{\epsilon}_s^i = \frac{F_{xy}^i + F_{yx}^i}{2};\ w^i = \frac{F_{xy}^i - F_{yx}^i}{2};\ \dot{\epsilon}_v^i = F_{xx}^i + F_{yy}^i. \tag{5}$$

For reference, the macroscopic deformation rates of the plane-shear configuration are $\dot{\gamma}/2$ for the shear strain rate and the vorticity and 0 for the volumetric strain rate.

Figure 4 shows that the microscopic deformations rate are, on average, equal to their macroscopic counterpart. However, they are widely distributed. Shear strain rate, and vorticity and volumetric strain rate all follow a normal distribution at high inertial number and transition to an exponential distribution at low inertial numbers, which is similar to the distribution of pair velocities. Figure 5 shows that their standard deviations $\sigma(\dot{\epsilon}_s^i)$, $\sigma(\dot{\epsilon}_v^i)$, and $\sigma(w^i)$ follow a similar power law of the inertial number,

$$\frac{\sigma(\dot{\epsilon}_s^i)}{1/t_i} \approx \frac{\sigma(\dot{\epsilon}_v^i)}{1/t_i} \approx \frac{\sigma(w^i)}{1/t_i} \propto \beta I^m, \tag{6}$$

with best-fit values of $\beta = 1.48$ and $m = 0.70$. Here, too, a power $m = 1$ would mean that all standard deviations would simply scale with the macroscopic shear rate $\dot{\gamma}$. A power less than one indicates that the inertial number affects these standard deviations, which become increasingly greater than $\dot{\gamma}$ at low inertial number. These distributions mean that there exist zones in the flow with a shear strain rate larger or smaller than the macroscopic one. Similarly, there exist zones rotating faster or slower than the macroscopic vorticity, and zones which are dilating or contracting while the flow is macroscopically neither dilating or contracting.

Figures 6(a)–6(i) evidence the spatial distributions of these three quantities. They highlight a spatially random distribution at high inertial number and large spatial correlations at low inertial number. Figures 6(j)–6(l) help one to visualize where the zones of extreme values of shear strain rate, volumetric strain rate, and vorticity coincide. They represent only grains with outlier values: $|x - \langle x \rangle| > 2\sigma(x)$, with x being either $\dot{\epsilon}_s^i$, $\dot{\epsilon}_v^i$, or w^i, $\langle \cdot \rangle$ the mean value of the distribution, and σ its standard deviation. These results show that at high inertial number zones of extreme vorticity, the volumetric and shear strain rates do not coincide and are rather seemingly randomly distributed within the flow. In contrast, they do coincide at low inertial number, where the flow features "hot" zones with extreme values of all three quantities and "cold" zones with close to average values of all of these quantities.

V. REPRESENTATIVE ELEMENTARY VOLUME

The distribution and spatial correlation of kinematic fields evidenced above suggest that microscopic strain rates spontaneously feature a mesoscopic organization at low inertial number. One could expect that their associated length scale constitutes a lower bound for the size of a representative elementary volume in these flows.

To determine the size of a REV, we propose the statistical method illustrated in Figs. 7(a) and 7(b). The flow is first split into square cells of size W. The standard deviation σ of a kinematic quantity ($\dot{\epsilon}_s$, $\dot{\epsilon}_v$, or w) is measured in each cell, and averaged over all cells and all time steps. We refer to the resulting averages $\langle \sigma(\dot{\epsilon}_s) \rangle$, $\langle \sigma(\dot{\epsilon}_v) \rangle$, and $\langle \sigma(w) \rangle$. A REV would exist if there is a finite cell size W_0 for which these quantities are similar to those measured in larger cells.

Figures 7(c)–7(e) show the evolution of these quantities with the cell size W. For the shear strain rate, the volumetric strain rate, and the vorticity, they are minimal for small cells ($W = 2d$). They gradually increase for larger cells before reaching a plateau. The explanation for this increase is that smaller cells are more likely to be fully contained within a hot zone or a cold zone. They would then include grains undergoing a similar kinematic, which yields small standard deviations within the cell. On the contrary, large cells are more likely to contain grains belonging to both hot and cold zones, featuring different kinematics.

As illustrated in Fig. 7(c), we propose to define a REV size W_0 as the cell size required to reach a mean standard deviation 95% of the maximum value: $\langle\sigma(W_0)\rangle = 0.95\langle\sigma(W = 40d)\rangle$. Taking the example of the shear strain rate, Fig. 7(c) shows that the REV size W_0 depends on the inertial number I: it becomes larger at lower inertial numbers.

Figure 7(f) presents the REV size W_0 obtained from the shear strain rate, volumetric strain rate, vorticity, and velocity fluctuations in the y direction. REV sizes related to the shear strain rate and vorticity are similar. They are generally larger than the REV size related to the volumetric strain rate. Accordingly, we propose to define the REV size of the flows based on shear strain rate and vorticity. Results are then consistent with a power law of the inertial number,

$$\frac{W_0}{d} \approx \zeta I^{n_R}, \tag{7}$$

with an exponent $n_R = -0.25$ and $\zeta = 4.5$. The REV size related to velocity fluctuations exhibits a power law with a similar exponent, but with a larger prefactor $\zeta = 9$. In the range of inertial numbers explored here, the REV size W_0 varies from a few grain diameters at high inertial numbers to a few dozen grain diameters at $I = 10^{-3}$. These values are dependent on the choice for the threshold (95%). Nonetheless, the REV results obtained with a different threshold (see Appendix A) show that this choice only affects the prefactor ζ, but not the power exponent n_R. Furthermore, Appendix B compares the value of the REV obtained with v_y with its spatial correlation length. While the REV size appears to be consistently larger than the correlation length, both quantities appear to increase as I decreases and diverge in the limit of $I \to 0$.

Extrapolating the law (7) to lower inertial number would lead to large REV sizes, for instance, $W_0 \approx 450d$ for $I = 10^{-8}$, a value commonly encountered in sheared fault gouge during earthquakes [29]. Experimental studies have revealed that REV dimensions for the volume fraction and energy dissipation in quasistatic flow conditions under simple shear are equal to $5d$ and $25d$, respectively [11]. Furthermore, for triaxial compression, a representative cubic element with a side length of $5.33d$ is introduced to capture the contact fabric, which is characterized by the coordination number and the contact fabric anisotropy [30]. The results presented here suggest that REV size based on internal kinematics may be much larger than these values in quasistatic flows. Further still, extrapolating our results to $\dot{\gamma} \to 0$ predicts a diverging REV size. This would correspond to an absence of a finite REV.

VI. CONCLUSION

This paper highlights a striking contrast between the macroscopic and microscopic deformation in granular flows. In macroscopically homogeneous shear flows, local strain rates are found to be widely distributed and spatially correlated, even more so at low inertial number. This observation resulted in the identification of a kinematics-based representative elementary volume, the size of which significantly increases and seemingly diverges at low inertial number. This REV size represents the characteristic size of instantaneous kinematic structures spontaneously developing within the flow.

This REV size is a fundamental piece of information to further develop homogenization theories explaining the effective behavior of granular flows as a continuum. It may be particularly useful to better understand the origin of finite-size effects. For instance, let us assume that constitutive laws for granular viscosity $\mu(I)$ and diffusivity $D(I)$ are measured in a large enough system—larger than the REV. The existence of a large REV size W_0 suggests that deviations from these laws could arise in flows at a distance from a boundary $h < W_0$, as kinematic structures would not have enough space to fully develop. The granular viscosity and diffusivity could then become a function of h: $\mu(I, h)$ and $D(I, h)$. Such deviations were indeed observed in experimental and simulated sheared flows in Refs. [6,21,22].

These results further suggest that large REV size may also develop in other soft materials which feature correlated particle motion; these include suspensions of grains [31–33], cohesive granular flows [34,35], foams [36,37], and suspensions of deformable particles (blood, emulsions) [38,39].

APPENDIX A: THE EFFECT OF THRESHOLD ON REV SIZE

Figure 8 shows the REV related to $\dot{\epsilon}_S$ obtained using two different thresholds: 95% and 90%. The results indicate that this choice is affecting the prefactor of the power law, but not its exponent.

APPENDIX B: COMPARING REV AND CORRELATION LENGTH

To measure the spatial correlation C of velocity in the y direction, we used the following expression:

$$C(\Delta) = \frac{< v_y^i v_y(y_i + \Delta) >}{< (v_y^i)^2 >}, \tag{B1}$$

where $< . >$ is an average over all grains i, v_y^i is the y velocity of that grain, and $v_y(y_i + \Delta)$ is the velocity at a distance Δ_y from the position of that grain. This velocity must be defined by some spatial average of the grain velocity near the position $(x_i; y_i + \Delta)$. We used the following coarse-graining function to estimate this average:

$$v_y(\Delta) = \frac{\sum_{j=1}^{n} v_y^j w(x_j - x_i, y_i + \Delta - y_j)}{\sum_{j=1}^{n} w(x_j - x_i, y_i + \Delta - y_j)}, \tag{B2}$$

with the weight function defined as

$$w(X, Y) = e^{-\frac{X^2+Y^2}{l^2}}. \tag{B3}$$

The length scale of the coarse graining l is set to be one grain diameter. Grains located much farther than l from the coordinate $(x_i; y_i + \Delta_y)$ will have virtually no influence on the coarse-grain velocity. Finally, the correlation length ℓ is defined as

$$\ell = \int_0^\infty C(\Delta)\partial\Delta, \tag{B4}$$

which is approximated by $\ell = \int_0^{20d} C(\Delta)\partial\Delta$. Figure 9 shows the autocorrelation function and compares the associated length scale ℓ to the REV (W_0). It appears that the REV size is consistently larger than the correlation length ℓ, but that both quantities diverge in the limit of $I \to 0$. This divergence is consistent with the results in Ref. [40].

[1] G. MiDi, On dense granular flows, Europhys. J. E **14**, 341 (2004).
[2] F. da Cruz, S. Emam, M. Prochnow, J.-N. Roux, and F. Chevoir, Rheophysics of dense granular materials: Discrete simulation of plane shear flows, Phys. Rev. E **72**, 021309 (2005).
[3] O. Pouliquen and Y. Forterre, A non-local rheology for dense granular flows, Philos. Trans. R. Soc. A: Math. Phys. Eng. Sci. **367**, 5091 (2009).
[4] K. Kamrin and G. Koval, Nonlocal constitutive relation for steady granular flow, Phys. Rev. Lett. **108**, 178301 (2012).
[5] M. Bouzid, M. Trulsson, P. Claudin, E. Clément, and B. Andreotti, Nonlocal rheology of granular flows across yield conditions, Phys. Rev. Lett. **111**, 238301 (2013).

[6] P. Kharel and P. Rognon, Vortices enhance diffusion in dense granular flows, Phys. Rev. Lett. **119**, 178001 (2017).
[7] R. Artoni, M. Larcher, J. T. Jenkins, and P. Richard, Self-diffusion scalings in dense granular flows, Soft Matter **17**, 2596 (2021).
[8] P. Rognon and M. Macaulay, Shear-induced diffusion in dense granular fluids, Soft Matter **17**, 5271 (2021).
[9] F. De Cola, A. Pellegrino, E. Barbieri, D. Penumadu, and N. Petrinic, Void ratio based representative volume element for modelling the high strain rate behaviour of granular materials, Intl. J. Impact Eng. **91**, 46 (2016).
[10] J. Wiącek and M. Molenda, Representative elementary volume analysis of polydisperse granular packings using discrete element method, Particuology **27**, 88 (2016).
[11] G. Shahin, E. B. Herbold, S. A. Hall, and R. C. Hurley, Quantifying the hierarchy of structural and mechanical length scales in granular systems, Extreme Mech. Lett. **51**, 101590 (2022).
[12] M. Costanza-Robinson, B. Estabrook, and D. Fouhey, Representative elementary volume estimation for porosity, moisture saturation, and air-water interfacial areas in unsaturated porous media: Data quality implications, Water Resour. Res. **47**, W07513 (2011).
[13] R. Al-Raoush and A. Papadopoulos, Representative elementary volume analysis of porous media using x-ray computed tomography, Powder Technol. **200**, 69 (2010).
[14] F. Radjai and S. Roux, Turbulentlike fluctuations in quasistatic flow of granular media, Phys. Rev. Lett. **89**, 064302 (2002).
[15] O. Pouliquen, Velocity correlations in dense granular flows, Phys. Rev. Lett. **93**, 248001 (2004).
[16] N. Mitarai and H. Nakanishi, Velocity correlations in dense granular shear flows: Effects on energy dissipation and normal stress, Phys. Rev. E **75**, 031305 (2007).
[17] E. DeGiuli, J. N. McElwaine, and M. Wyart, Phase diagram for inertial granular flows, Phys. Rev. E **94**, 012904 (2016).
[18] T. Hagemeier, M. Börner, A. Bück, and E. Tsotsas, A comparative study on optical techniques for the estimation of granular flow velocities, Chem. Eng. Sci. **131**, 63 (2015).
[19] Y. Cao, J. Li, B. Kou, C. Xia, Z. Li, R. Chen, H. Xie, T. Xiao, W. Kob, L. Hong *et al.*, Structural and topological nature of plasticity in sheared granular materials, Nat. Commun. **9**, 2911 (2018).
[20] J. Gaume, G. Chambon, and M. Naaim, Microscopic origin of nonlocal rheology in dense granular materials, Phys. Rev. Lett. **125**, 188001 (2020).
[21] T. Miller, P. Rognon, B. Metzger, and I. Einav, Eddy viscosity in dense granular flows, Phys. Rev. Lett. **111**, 058002 (2013).
[22] P. G. Rognon, T. Miller, B. Metzger, and I. Einav, Long-range wall perturbations in dense granular flows, J. Fluid Mech. **764**, 171 (2015).
[23] R. Artoni and P. Richard, Effective wall friction in wall-bounded 3d dense granular flows, Phys. Rev. Lett. **115**, 158001 (2015).
[24] A. Lees and S. Edwards, The computer study of transport processes under extreme conditions, J. Phys. C **5**, 1921 (1972).
[25] A. Singh, V. Magnanimo, K. Saitoh, and S. Luding, The role of gravity or pressure and contact stiffness in granular rheology, New J. Phys. **17**, 043028 (2015).
[26] M. Macaulay and P. Rognon, Inertial force transmission in dense granular flows, Phys. Rev. Lett. **126**, 118002 (2021).
[27] S. Kim and K. Kamrin, Power-law scaling in granular rheology across flow geometries, Phys. Rev. Lett. **125**, 088002 (2020).
[28] P. Marmottant, C. Raufaste, and F. Graner, Discrete rearranging disordered patterns, Part II: 2d plasticity, elasticity and flow of a foam, Europhys. J. E **25**, 371 (2008).
[29] E. Papachristos, I. Stefanou, and J. Sulem, A discrete elements study of the frictional behavior of fault gouges, J. Geophys. Res.: Solid Earth **128**, e2022JB025209 (2023).
[30] S. Schmidt, M. Wiebicke, and I. Herle, On the determination and evolution of fabric in representative elementary volumes for a sand specimen in triaxial compression, Granular Matter **24**, 97 (2022).

[31] E. C. Eckstein, D. G. Bailey, and A. H. Shapiro, Self-diffusion of particles in shear flow of a suspension, J. Fluid Mech. **79**, 191 (1977).
[32] A. Sierou and J. F. Brady, Shear-induced self-diffusion in non-colloidal suspensions, J. Fluid Mech. **506**, 285 (1999).
[33] B. Metzger, O. Rahli, and X. Yin, Heat transfer across sheared suspensions: Role of the shear-induced diffusion, J. Fluid Mech. **724**, 527 (2013).
[34] M. Macaulay and P. Rognon, Shear-induced diffusion in cohesive granular flows: Effect of enduring clusters, J. Fluid Mech. **858**, R2 (2019).
[35] S.-S. Hsiau, L.-S. Lu, C.-Y. Chou, and W.-L. Yang, Mixing of cohesive particles in a shear cell, Intl. J. Multiphase Flow **34**, 352 (2008).
[36] M. Sexton, M. Möbius, and S. Hutzler, Bubble dynamics and rheology in sheared two-dimensional foams, Soft Matter **7**, 11252 (2011).
[37] S. Cohen-Addad, R. Höhler, and O. Pitois, Flow in foams and flowing foams, Annu. Rev. Fluid Mech. **45**, 241 (2013).
[38] M. Gross, T. Kruger, and F. Varnik, Fluctuations and diffusion in sheared athermal suspensions of deformable particles, Europhys. Lett. **108**, 68006 (2014).
[39] J. Tang, S. E. Erdener, B. Li, B. Fu, S. Sakadzic, S. A. Carp, J. Lee, and D. A. Boas, Shear-induced diffusion of red blood cells measured with dynamic light scattering-optical coherence tomography, J. Biophoton. **11**, e201700070 (2018).
[40] K. Saitoh and H. Mizuno, Anomalous energy cascades in dense granular materials yielding under simple shear deformations, Soft Matter **12**, 1360 (2016).